

MULTI-TEV GAMMA-RAY OBSERVATION FROM THE CRAB NEBULA
USING THE TIBET-III AIR SHOWER ARRAY
FINELY TUNED BY THE COSMIC-RAY MOON'S SHADOW

M. AMENOMORI¹, X. J. BI², D. CHEN³, S. W. CUI⁴, DANZENGLUOBU⁵, L. K. DING², X. H. DING⁵, C. FAN⁶, C. F. FENG⁶, ZHAOYANG FENG², Z. Y. FENG⁷, X. Y. GAO⁸, Q. X. GENG⁸, H. W. GUO⁵, H. H. HE², M. HE⁶, K. HIBINO⁹, N. HOTTA¹⁰, HAIBING HU⁵, H. B. HU², J. HUANG^{2,3}, Q. HUANG⁷, H. Y. JIA⁷, F. KAJINO¹¹, K. KASAHARA¹², Y. KATAYOSE¹³, C. KATO¹⁴, K. KAWATA³, LABACIREN⁵, G. M. LE¹⁵, A. F. LI⁶, J. Y. LI⁶, Y.-Q. LOU¹⁶, H. LU², S. L. LU², X. R. MENG⁵, K. MIZUTANI^{12,17}, J. MU⁸, K. MUNAKATA¹⁴, A. NAGAI¹⁸, H. NANJO¹, M. NISHIZAWA¹⁹, M. OHNISHI³, I. OHTA²⁰, H. ONUMA¹⁷, T. OUCHI⁹, S. OZAWA¹², J. R. REN², T. SAITO²¹, T. Y. SAITO²², M. SAKATA¹¹, T. K. SAKO³, M. SHIBATA¹³, A. SHIOMI²³, T. SHIRAI⁹, H. SUGIMOTO²⁴, M. TAKITA³, Y. H. TAN², N. TATEYAMA⁹, S. TORII¹², H. TSUCHIYA²⁵, S. UDO¹², B. WANG², H. WANG², X. WANG¹², Y. WANG², Y. G. WANG⁶, H. R. WU², L. XUE⁶, Y. YAMAMOTO¹¹, C. T. YAN³, X. C. YANG⁸, S. YASUE²⁶, Z. H. YE¹⁵, G. C. YU⁷, A. F. YUAN⁵, T. YUDA⁹, H. M. ZHANG², J. L. ZHANG², N. J. ZHANG⁶, X. Y. ZHANG⁶, Y. ZHANG², YI ZHANG², ZHAXISANGZHU⁵ AND X. X. ZHOU⁷

(THE TIBET AS γ COLLABORATION)

Draft Version

ABSTRACT

The Tibet-III air shower array, consisting of 533 scintillation detectors, has been operating successfully at Yangbajing in Tibet, China since 1999. Using the dataset collected by this array from 1999 November through 2005 November, we obtained the energy spectrum of γ -rays from the Crab Nebula, expressed by a power law as $(dJ/dE) = (2.09 \pm 0.32) \times 10^{-12} (E/3 \text{ TeV})^{-2.96 \pm 0.14} \text{ cm}^{-2} \text{ s}^{-1} \text{ TeV}^{-1}$ in the energy range of 1.7 to 40 TeV. This result is consistent with other independent γ -ray observations by imaging air Cherenkov telescopes. In this paper, we carefully checked and tuned the performance of the Tibet-III array using data on the moon's shadow in comparison with a detailed Monte Carlo simulation. The shadow is shifted to the west of the moon's apparent position as an effect of the geomagnetic field, although the extent of this displacement depends on the primary energy positively charged cosmic rays. This finding enables us to estimate the systematic error in determining the primary energy from its shower size. This error is estimated to be less than $\pm 12\%$ in our experiment. This energy scale estimation is the first attempt among cosmic-ray experiments at ground level. The systematic pointing error is also estimated to be smaller than $0^{\circ}011$. The deficit rate and position of the moon's shadow are shown to be very stable within a statistical error of $\pm 6\%$ year by year. This guarantees the long-term stability of point-like source observation with the Tibet-III array. These systematic errors are adequately taken into account in our study of the Crab Nebula.

Subject headings: cosmic rays — gamma rays : observations — magnetic fields — Moon — pulsars : individual (Crab pulsar) — supernova remnants : individual (Crab Nebula)

1. INTRODUCTION

The Crab Nebula is a standard source of radiation in the northern sky across a wide energy band, from radio to near 100 TeV γ -rays. It is well known that the multi-wavelength non-thermal energy spectrum is dominated by synchrotron radiation at energies lower than 1 GeV

¹⁵ Center of Space Science and Application Research, Chinese Academy of Sciences, Beijing 100080, China.

¹⁶ Physics Department and Tsinghua Center for Astrophysics, Tsinghua University, Beijing 100084, China.

¹⁷ Department of Physics, Saitama University, Saitama 338-8570, Japan.

¹⁸ Advanced Media Network Center, Utsunomiya University, Utsunomiya 321-8585, Japan.

¹⁹ National Institute of Informatics, Tokyo 101-8430, Japan.

²⁰ Sakushin Gakuin University, Utsunomiya 321-3295, Japan.

²¹ Tokyo Metropolitan College of Industrial Technology, Tokyo 116-8523, Japan.

²² Max-Planck-Institut für Physik, München D-80805, Deutschland.

²³ College of Industrial Technology, Nihon University, Narashino 275-8576, Japan.

²⁴ Shonan Institute of Technology, Fujisawa 251-8511, Japan.

²⁵ RIKEN, Wako 351-0198, Japan.

²⁶ School of General Education, Shinshu University, Matsumoto 390-8621, Japan.

¹ Department of Physics, Hirosaki University, Hirosaki 036-8561, Japan.

² Key Laboratory of Particle Astrophysics, Institute of High Energy Physics, Chinese Academy of Sciences, Beijing 100049, China.

³ Institute for Cosmic Ray Research, University of Tokyo, Kashiwa 277-8582, Japan.

⁴ Department of Physics, Hebei Normal University, Shijiazhuang 050016, China.

⁵ Department of Mathematics and Physics, Tibet University, Lhasa 850000, China.

⁶ Department of Physics, Shandong University, Jinan 250100, China.

⁷ Institute of Modern Physics, SouthWest Jiaotong University, Chengdu 610031, China.

⁸ Department of Physics, Yunnan University, Kunming 650091, China.

⁹ Faculty of Engineering, Kanagawa University, Yokohama 221-8686, Japan.

¹⁰ Faculty of Education, Utsunomiya University, Utsunomiya 321-8505, Japan.

¹¹ Department of Physics, Konan University, Kobe 658-8501, Japan.

¹² Research Institute for Science and Engineering, Waseda University, Tokyo 169-8555, Japan.

¹³ Faculty of Engineering, Yokohama National University, Yokohama 240-8501, Japan.

¹⁴ Department of Physics, Shinshu University, Matsumoto 390-8621, Japan.

and by the inverse-Compton scattering above 1 GeV (De Jager et al. 1996; Atoyan & Aharonian 1996).

TeV γ -rays from the Crab Nebula were first clearly detected by the Whipple collaboration using an imaging air Cherenkov telescope (IACT) in 1989 (Weekes et al. 1989). Since then, IACT has become the standard telescope for high-energy γ -ray observations by virtue of its excellent angular resolution and efficiency. Many IACTs have been constructed and are operating around the world, detecting about 70 γ -ray sources in total up to the present. On the other hand, air shower arrays have been constructed to search for γ -rays from point sources at high altitude. The merit of this technique is that it can be operated for 24 hours every day, regardless of weather, with a wide field of view of about 2 sr. The energy threshold of the γ -rays detected is higher than that of IACTs, say about 3 TeV at high altitude. Among these instruments, the Tibet AS γ Collaboration achieved the first successful observation of the Crab Nebula at a multi-TeV region in 1999, using a so-called HD (high density) array in which 109 scintillation detectors were deployed at 7.5 m spacing lattice intervals in an area of 5,175 m² (Amenomori et al. 1999a). The Milagro group also reported the detection of TeV γ -ray signals from the Crab Nebula using a water Cherenkov pool (Atkins et al. 2003).

Recently, IACTs have obtained updated information on the Crab Nebula. The HEGRA experiment has extended the nebula's energy spectrum up to 80 TeV with an approximate power-law shape, after patient observation for almost 400 hours in total (Aharonian et al. 2004). In contrast, the MAGIC experiment, equipped with the world's largest tessellated reflector (17 m in diameter), has successfully observed the lower energy part of the spectrum down to 77 GeV (Albert et al. 2008). The H.E.S.S. group examined the energy spectra of the Crab Nebula obtained from various IACTs (Whipple, HEGRA, CAT and H.E.S.S.) to evaluate the systematic errors of these instruments (Aharonian et al. 2006). Their fluxes are well in agreement with one another within the statistical and systematic errors at the moderate energy region, although the cutoff energy and spectral index seem to differ somewhat. Thus, the Crab Nebula has been well studied by various techniques and has been used as a standard calibration source among the ground-based γ -ray experiments in the TeV region.

The energy of a primary cosmic-ray particle is estimated by observing the number of secondary particles in an air shower experiment as well as the number of Cherenkov photons for IACTs, and then by comparing these values against the results of detailed Monte Carlo simulations, including the detector structure and response. The most conventional method for estimating the absolute energy scale of primary particles may be to compare the flux values between the direct (satellite/balloon-borne) and indirect observations. The cosmic-ray flux, however, depends inevitably on the detection technique, analysis method, detector simulation, and so on. Therefore, it is very important to develop a new method for directly estimating the absolute energy scale in an air shower experiment at TeV energies.

Clark (1957) anticipated in 1957 that the sun and the moon, each with a finite size of 0.5 in diameter,

cast shadows in the high-energy cosmic-ray flux, respectively. Actually, the shadowing effect of the sun and the moon (hereafter, we call these the sun's shadow and the moon's shadow, respectively) was observed by air shower experiments in the 1990s (Alexandreas 1991; Amenomori et al. 1993), and the sharpness of the observed shadows was used to estimate their angular resolutions experimentally. In particular, the Tibet air shower array, with its high event trigger rate and good angular resolution, enables us to use the geomagnetic field as a magnetic spectrometer for primary cosmic rays at multi-TeV energies. As almost all primary cosmic rays are positively charged, they are bent eastward by the geomagnetic field at Yangbajing in Tibet. The moon's shadow should then be observed in the west of the moon's apparent position, although the position of the shadow in relation to that of the moon depends on the cosmic-ray energy (Amenomori et al. 2000a). Hence, the position and the shape of the moon's shadow allow us to estimate the possible systematic error in the absolute energy scale of observed showers. Until now, the pointing accuracy and angular resolution of the Tibet-III array have been checked by monitoring the moon's shadow continuously month by month (Amenomori et al. 2003). It is also worthwhile to note that the moon's and sun's shadows provide information about the cosmic-ray \bar{p}/p flux ratio (Achard et al. 2005; Amenomori et al. 2007a) and the global structure of the interplanetary magnetic field between the sun and the earth (Amenomori et al. 1993; Amenomori et al. 1994; Amenomori et al. 1999b; Amenomori et al. 2000a).

In this paper, we first discuss the systematic uncertainties of the Tibet-III array and a new method for calibrating the absolute energy of primary particles in the multi-TeV energy region using the moon's shadow data. Based on the results, we report on the γ -ray observation of the Crab Nebula and search for pulsed γ -ray emissions from the Crab pulsar using the dataset obtained by the Tibet-III array.

2. EXPERIMENT

2.1. Tibet-III Air Shower Array

The Tibet-III array shown in Figure 1 was completed on the basis of the success of the Tibet-I, II and II/HD experiments (Amenomori et al. 1992; Amenomori et al. 1999a; Amenomori et al. 2000b) in the late fall of 1999. This array consists of 533 scintillation detectors of 0.5 m², and the detectors on the inner side of the array are placed on a lattice with 7.5 m spacing, covering 22,050 m². A lead plate 0.5 cm thick is placed on top of each detector to improve the angular resolution. Using this array, we succeeded in observing γ -ray flares from Mrk 421 and found a correlation between TeV γ -ray and X-ray intensities (Amenomori et al. 2003). In 2002 and 2003, the inside area of the Tibet-III array was further enlarged to 36,900 m² by adding 256 detectors. This full Tibet-III array has been successfully operating since 2003. In this paper, to keep the form of the data the same throughout the observation period from 1999 to 2005, we reconstructed air shower data obtained from the detector configuration shown in Figure 1 even for the full Tibet-III array.

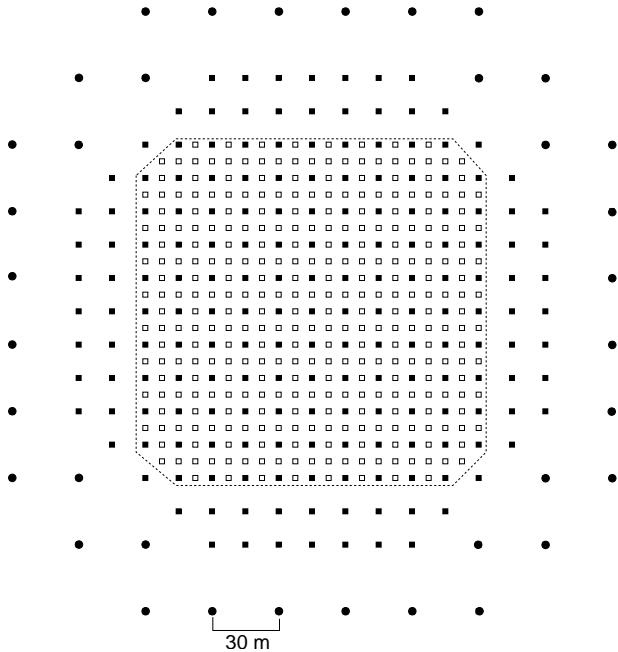


FIG. 1.— Schematic view of the Tibet-III array operating at Yangbajing. Open squares: FT detectors equipped with a fast-timing (FT) photomultiplier tube (PMT); filled squares: FT detectors with a wide dynamic-range PMT; filled circles: density detectors with a wide-dynamic range PMT. We have selected air shower events whose cores are located within the detector matrix enclosed by the dotted line.

2.2. Event Reconstruction

The raw data obtained from the Tibet-III array system mainly consist of the following: a trigger time stamp for each event from a global positioning system (GPS) clock supplemented by a computer clock; timing and charge information from each hit PMT, digitized by a time-to-digital converter (TDC) and a charge-sensitive analog-to-digital converter (ADC); and calibration data taken every 20 minutes. The ADC and TDC counts are then converted to the number of particles and the relative timing for each detector, respectively, using the calibration data. An air shower event is reconstructed as follows.

The core position of each air shower is estimated using the lateral distribution of the number of shower particles observed in the array. The density-weighted position of the air shower core on the surface of the Tibet-III array is calculated as $(X_{\text{core}}, Y_{\text{core}}) = \left(\frac{\sum_i \rho_i^2 x_i}{\sum_i \rho_i^2}, \frac{\sum_i \rho_i^2 y_i}{\sum_i \rho_i^2} \right)$, where x_i and y_i are the coordinates of the i -th detector and ρ_i is the number density (m^{-2}) of detected particles. In this analysis, we regard the shower size $\sum \rho_{\text{FT}}$ as the primary energy reference, where size $\sum \rho_{\text{FT}}$ is defined as the sum of the number of particles per m^2 for each FT detector. For γ -ray-induced air showers, overall core position resolutions are then estimated as 12 m and 4 m at median for $\sum \rho_{\text{FT}} < 100$ and $\sum \rho_{\text{FT}} > 100$, respectively.

The arrival direction of each shower is estimated assuming that the front of the air shower is conical shape. The apex of a cone is then taken to be the estimated core position $(X_{\text{core}}, Y_{\text{core}})$. The average delay time T (ns) of shower particles is expressed as a function of the distance R (m) from the core position as $T = 0.075R$, which is optimized by simulations. This gives a cone slope of $1:3$ with respect to the plane perpendicular to the air shower arrival direction.

2.3. Event Selection

An event trigger signal is issued when an any-fourfold coincidence appears in the FT detectors that have each recorded more than 0.6 particles within a coincidence gate width of 600 ns, resulting in a trigger rate of about 680 Hz. We collected 2.0×10^{10} events during 1318.9 live days from 1999 November 18 through 2005 November 15 after some quality cuts and event selection based on three simple criteria: (1) each shower event should fire four or more FT detectors that have each recorded 1.25 or more particles; (2) among the 9 hottest FT detectors in each event, 8 should be contained in the fiducial area enclosed by the dotted line in Figure 1. If fewer than 9 detectors have been hit, they should all be contained in the fiducial area; and (3) the zenith angle of the event arrival direction should be less than 40° . After these criteria have been met, the overall angular resolution and the modal energy of air shower events, thus obtained, are better than 1 degree and about 3 TeV, respectively (Amenomori et al. 2003), thereby covering the upper portion of the energies measured by IACTs.

3. MOON'S SHADOW AND PERFORMANCE OF THE TIBET-III AIR SHOWER ARRAY

3.1. Analysis

Using the dataset described in §2.3, we further select the events within a circle of the radius 5° centered at the moon; this circle is defined as the on-source field. An equatorial coordinate system is defined, fixing the origin of coordinates at the moon's center. To estimate the background against deficits in the moon's shadow, we adopt the equi-zenith angle method (Amenomori et al. 2003; Amenomori et al. 2005), which is also used for the Crab Nebula observation described in §4.1. Eight off-source fields are symmetrically aligned on both sides of the on-source field, at the same zenith angle. In order to avoid deficit events that are affected by background event contamination of the on-source field, the nearest two off-source fields are each set at an angular distance $9^\circ 6'$ from the on-source field. Other off-source fields are located every $3^\circ 2'$ from the nearest off-source fields. The position of each observed event in an on-/off-source field is then specified by the angular distance θ and the position angle ϕ , where θ and ϕ are measured from the center and from the north direction, respectively. Using θ and ϕ , the on-/off-source fields are meshed by $0^\circ 05' \times 0^\circ 05'$ cells, and we count the number of events in each cell. To maximize the S/N ratio, we group the cells into new on-/off-source bins according to the angular resolution, which depends on the shower size $\sum \rho_{\text{FT}}$. The angular resolution becomes worst at a threshold energy of around 1 TeV. This value is, however, smaller than half of the angular distance between two adjoining off-source bins, i.e., $\sim 1^\circ 6'$, so that off-source bins never overlap mutually in this background analysis.

We calculate the statistical significance of deficits or signals using the formula (Li & Ma 1983) $(N_{\text{ON}} - \epsilon N_{\text{OFF}}) / \sqrt{\epsilon(N_{\text{ON}} + N_{\text{OFF}})}$, where N_{ON} and N_{OFF} are the number of events in the on-source bin and the number of background events summed over 8 off-source bins, respectively, and ϵ is the ratio of the on-source solid angle area to the off-source solid angle area ($\epsilon = 1/8$ in this

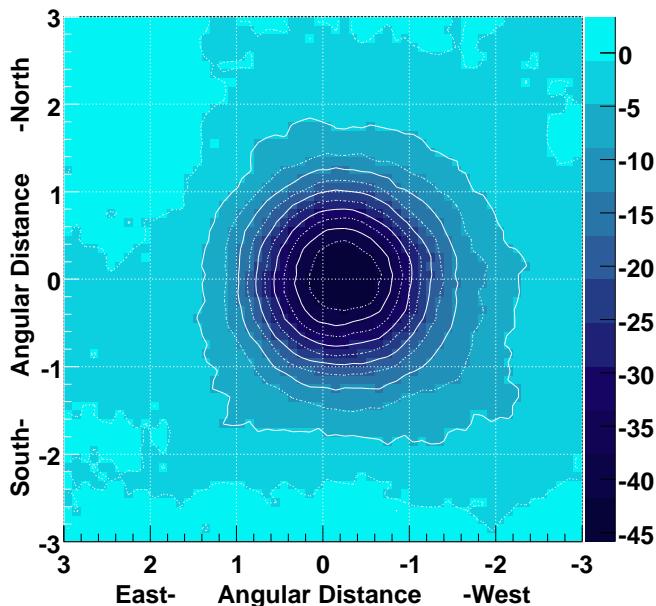


FIG. 2.— Significance map of the deficit event densities observed by the Tibet-III array for 1318.9 live days, made using the events with $\sum \rho_{\text{FT}} > 10^{1.25}$ ($> \sim 2$ TeV), in the square area of $6^\circ \times 6^\circ$ whose origin is at the apparent center of the moon. The scale at right shows the level of significance of the deficit event density in terms of the standard deviation σ .

work).

In order to investigate the energy dependence, the shower size $\sum \rho_{\text{FT}}$ is divided by 1/4 decades in $10 < \sum \rho_{\text{FT}} \leq 100$, and by 1/3 decades in $100 < \sum \rho_{\text{FT}} \leq 1000$, where the lowest air shower size bin is omitted from the analysis, because it is close to the energy threshold of the Tibet-III array and the trigger efficiency is estimated to be very low ($< 1\%$). Hereafter, this partition is commonly used in observations of both the moon's shadow and the Crab Nebula.

Figure 2 shows the experimental significance map of the deficit event densities observed with the Tibet-III array for 1318.9 live days. This map is smoothed using the events with $\sum \rho_{\text{FT}} > 10^{1.25}$ ($> \sim 2$ TeV) within a circle of radius 0.9 , corresponding to the overall angular resolution for these events. The maximum deficit reaches the significance level of 45σ at the center. It is seen that the center of the observed moon's shadow is shifted to the west by about 0.2 due to the effect of the geomagnetic field.

3.2. Monte Carlo Simulation of the Moon's Shadow

We have performed a detailed Monte Carlo (MC) simulation of the moon's shadow. For the geomagnetic field, we adopt the International Geomagnetic Reference Field (IGRF) 9th generation model (Macmillan et al. 2003) at an altitude < 600 km, and connect it to the dipole moment model at an altitude > 600 km. For the primary particles, we use the chemical composition obtained mainly from the data of direct observations (Asakimori et al. 1998; Sanuki et al. 2000; Apanasenko et al. 2001; Amenomori et al. 2008) in the energy range of 0.3 TeV to 1000 TeV. The minimum energy of primary particles is set to 0.3 TeV, which is

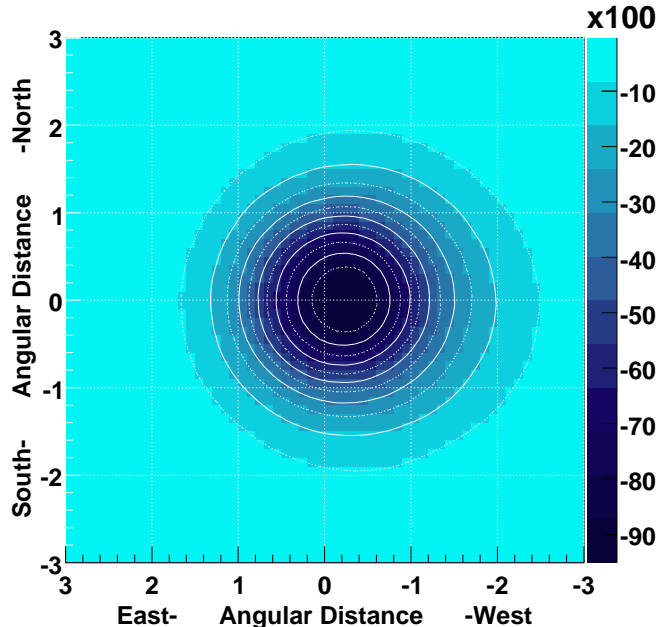


FIG. 3.— Deficit event density map obtained by the MC simulation. The events with $\sum \rho_{\text{FT}} > 10^{1.25}$ ($> \sim 2$ TeV) are plotted in the square area of $6^\circ \times 6^\circ$. The map is made in the same way as in Figure 2, and the scale at right represents the deficit event density (degree^{-2}).

low enough to cover the threshold energy of our trigger condition. Air shower events are generated at the top of the atmosphere along the moon's orbit around the earth, using the CORSIKA code (Heck et al. 1998) with QGSJET or SIBYLL interaction models. The air shower core of each simulated event is uniformly distributed over a circular region with a 300 m radius centered at the array; this circle sufficiently covers the area where cosmic-ray events are actually triggered in our array. Air shower particles generated by primary particles in the atmosphere are traced until their energies reach 1 MeV. In order to treat the MC events in the same way as the events in the experimental data, these simulated events are distributed among the detectors in the same detector configuration as in the Tibet-III array by the Epics code (Amenomori et al. 2008; Kasahara), and are converted to the same format as the experimental dataset, such as the ADC and TDC values at each detector. After air shower reconstruction analysis and data selection, we assign the opposite charge to the remaining primary particles. These anti-particles are randomly shot back toward directions within $20^\circ \times 20^\circ$ centered at the moon from the first interaction point of the air shower. Hereafter, we call this the initial shooting direction. The particle track influenced by the geomagnetic field between the earth and the moon is calculated by the Runge-Kutta method of order 4 based on the Lorentz force. If the primary particle hits the moon, its initial shooting direction should be equivalent to the observed particle direction shielded by the moon. Otherwise, it is shot back in another direction and the particle track is calculated again. This routine continues until almost all particles have hit the moon. Finally, these initial shooting directions are smeared by the angular resolution event by event. In this way, the expected moon's shadow is equivalent to

the observed moon's shadow. Figure 3 shows the event map of the moon's shadow calculated by the MC simulation for events with $\sum \rho_{\text{FT}} > 10^{1.25}$ ($> \sim 3$ TeV). This map is smoothed using the events within a circle of radius $0^\circ.9$, corresponding to the overall angular resolution for events with $\sum \rho_{\text{FT}} > 10^{1.25}$. The MC simulation well reproduces the observed moon's shadow, as shown in Figure 2.

3.3. Shape of the Moon's Shadow and Performance of the Tibet-III Array

The filled circles in Figure 4 (a)–(f) show the observed deficit counts around the moon projected onto the east-west axis for each $\sum \rho_{\text{FT}}$ bin, where $\sum \rho_{\text{FT}}$ is the shower size defined as the sum of the number of particles per m^2 for each FT detector. The representative cosmic-ray energy in each $\sum \rho_{\text{FT}}$ bin is defined as be the logarithmic mean of the energy E divided by the atomic number Z , assuming the cosmic-ray composition spectrum described in §3.2. In these figures, it is seen that the peak position of the deficit counts gradually shifts to the west as primary energy decreases due to the influence of the geomagnetic field. Also, the deficit counts become narrower as primary energy increases, since the angular resolution increases roughly in inverse proportion to $\sqrt{\sum \rho_{\text{FT}}}$. The MC results (histograms) are compared with the experimental data at various size intervals in Figure 4, and are in good agreement with the experimental data.

In order to estimate the peak position of the observed moon's shadow, we use the shadow shape obtained by the MC simulation. We first express the MC shadows shown in Figure 4 with the superposition of two Gaussian functions using the least χ^2 method as,

$$f_{\text{MC}}(\theta) = G_1(\theta; a_1, m_1, \sigma_1) + G_2(\theta; a_2, m_2, \sigma_2), \quad (1)$$

where $G_i(\theta; a_i, m_i, \sigma_i) = a_i e^{-(\theta - m_i)^2 / \sigma_i^2}$ and θ is the angular distance from the moon. Here, a_1 , a_2 , m_1 , m_2 , σ_1 and σ_2 are the fitting parameters denoting the amplitudes, means and one-standard deviations of the double Gaussian, respectively. It is found that the shadows (e) and (f) can be expressed by a single Gaussian, while the others are expressed by a double Gaussian.

Using these fitting parameters, we then estimate the peak position of the observed shadow as follows. Keeping the form of function $f_{\text{MC}}(\theta)$, we express the observed shadow by the equation,

$$f_{\text{Data}}(\theta) = G_1(\theta; A_1, M_1, \sigma_1) + G_2(\theta; A_1 \times (a_2/a_1), M_1 + (m_2 - m_1), \sigma_2), \quad (2)$$

where A_1 and M_1 denote the amplitude and mean of the Gaussian, respectively, and are free parameters, while the others are the coefficients calculated by fitting equation (1). Using equation (2), we can estimate the peak position of the moon's shadow.

We also confirm that the east-west component of the geomagnetic field strength is negligible in the part of the sky where the moon is visible by the Tibet-III array. This means that the north-south displacement of the moon's shadow observed by the Tibet-III array does not depend on the geomagnetic field. The displacement of the peak of the moon's shadow in the north-south direction then enables us to estimate the magnitude of the array's systematic pointing error. Figure 5 shows the

energy dependence of the displacement of the moon's shadow in the north-south direction. The filled circles denote the experimental data, and the open squares are the MC results. The MC simulation well reproduces the experimental data. A χ^2 fitting to the data gives $0^\circ.008 \pm 0^\circ.011$ assuming a constant function independent of energy. From this, the systematic pointing error is estimated to be smaller than $0^\circ.011$.

3.4. Calibration of Primary Particle Energy and Systematic Errors

Figure 6 shows the shower size dependence of the displacement of the moon's shadow in the east-west direction, obtained by fitting Figure 4. In this figure, the open squares show the MC results using the QGSJET model, and are quite consistent with the experimental data. The upper scale indicates the logarithmic mean of the energy E divided by the atomic number Z (TeV/Z), i.e., $\langle \log(E/Z) \rangle$, in each $\sum \rho_{\text{FT}}$ bin. One can see that the position of the moon's shadow gradually shifts to the west as the primary energy decreases due to the influence of the geomagnetic field. Hence, the absolute energy scale of cosmic rays observed by the Tibet-III array can be directly checked by using the geomagnetic field as a magnetic spectrometer, as we now discuss.

First, the MC simulation points are fitted by the function $\kappa(\sum \rho_{\text{FT}}/100)^\lambda$ to define a standard curvature function, resulting in $\kappa = -0.183$ and $\lambda = -0.720$, as shown by a solid curve in Figure 6, where the MC statistical errors are negligible compared with the experimental data.

Second, the experimental data (filled circles) are fitted by this standard curvature function with the $\sum \rho_{\text{FT}}$ shift term

$$-0.183 [(1 - \Delta R_S)(\sum \rho_{\text{FT}}/100)]^{-0.720}, \quad (3)$$

to estimate the possible shift in the $\sum \rho_{\text{FT}}$ between the experimental data and the MC simulation, as shown by the solid curve in Figure 6, where ΔR_S is the $\sum \rho_{\text{FT}}$ shift ratio, resulting in $\Delta R_S = (-4.9 \pm 9.5)\%$. We should then convert ΔR_S to the energy shift ratio ΔR_E as a final result. To determine the relationship between ΔR_S and ΔR_E , and to confirm that this method is sensitive to energies, we prepare six kinds of MC event samples in which the energy of the primary particles is systematically shifted event by event in the moon's shadow simulation. These six ΔR_E s are $\pm 20\%$, $\pm 15\%$ and $\pm 8\%$, respectively. In each MC event sample, the $\sum \rho_{\text{FT}}$ dependence of the displacement of the moon's shadow is calculated in the same way, and the $\sum \rho_{\text{FT}}$ shift ratio ΔR_S is estimated by fitting the data to equation (3). Finally, we get the relation $\Delta R_E = (-0.91 \pm 0.05) \Delta R_S$ assuming a linear function. Hence, the systematic error in the absolute energy scale ΔR_E with statistical error σ_{stat} is estimated to be $(+4.5 \pm 8.6_{\text{stat}})\%$.

Furthermore, we investigate two kinds of systematic uncertainties with the proposed method. One is that the position of the moon's shadow by the MC simulation depends on the assumed primary cosmic-ray composition. In this simulation, the chemical composition ratio of primary cosmic rays is estimated based mainly on the data obtained by direct observations. These datasets should also have statistical and systematic errors. The position of the moon's shadow is dominated by the light

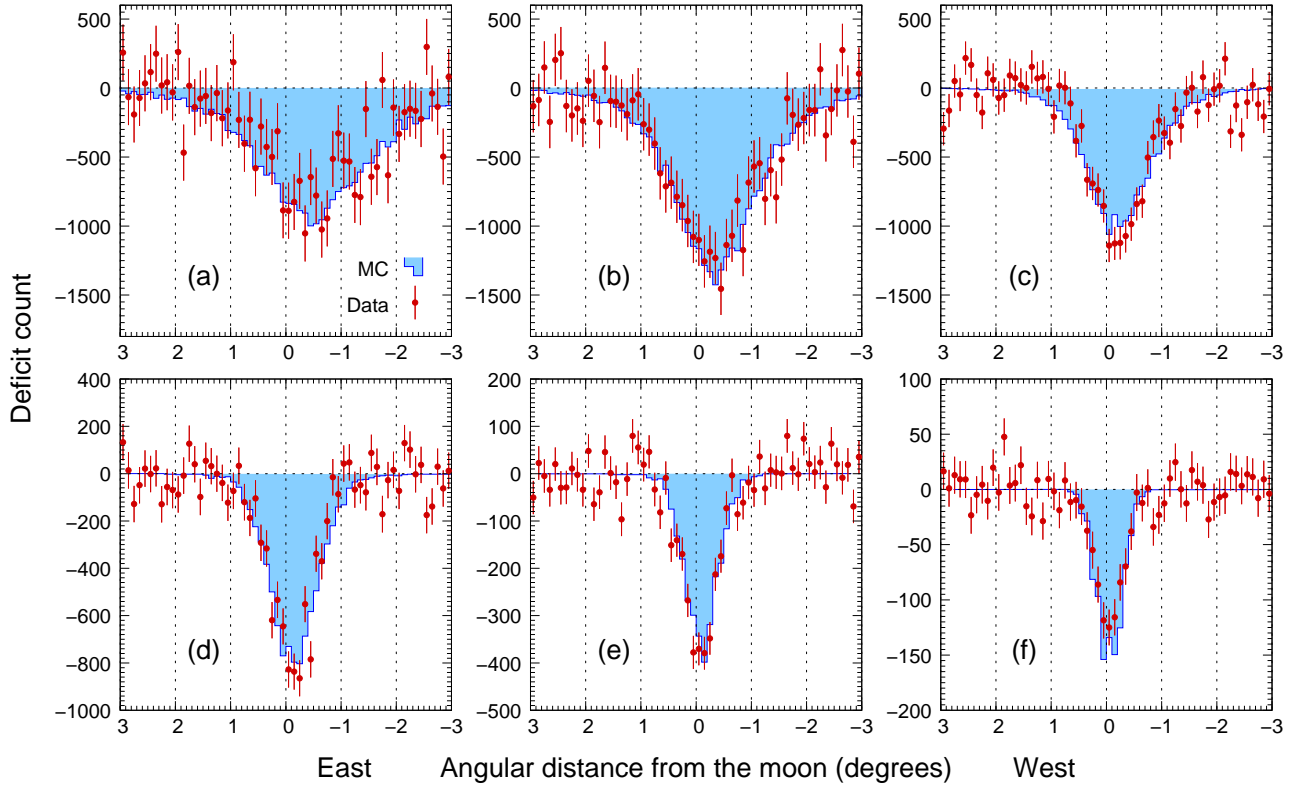


FIG. 4.— Filled circles show experimental data for deficit counts around the moon projected to the east-west axis for each $\sum \rho_{\text{FT}}$ bin. We use the events contained in the angular band, centered at and parallel to the east-west axis, comparable to the $\sum \rho_{\text{FT}}$ -dependent angular resolution: (a): $\pm 1^\circ 4$ for 2.94 TeV/Z in $10^{1.25} < \sum \rho_{\text{FT}} \leq 10^{1.50}$; (b): $\pm 1^\circ 0$ for 4.20 TeV/Z in $10^{1.50} < \sum \rho_{\text{FT}} \leq 10^{1.75}$; (c): $\pm 0^\circ 7$ for 6.46 TeV/Z in $10^{1.75} < \sum \rho_{\text{FT}} \leq 10^{2.00}$; (d): $\pm 0^\circ 5$ for 11.4 TeV/Z in $10^{2.00} < \sum \rho_{\text{FT}} \leq 10^{2.33}$; (e): $\pm 0^\circ 3$ for 21.6 TeV/Z in $10^{2.33} < \sum \rho_{\text{FT}} \leq 10^{2.67}$; (f): $\pm 0^\circ 2$ for 45.4 TeV/Z in $10^{2.67} < \sum \rho_{\text{FT}} \leq 10^{3.00}$. The solid histograms denote the moon's shadow simulation assuming the primary cosmic-ray composition based on direct observations (Asakimori et al. 1998; Sanuki et al. 2000; Apanasenko et al. 2001; Amenomori et al. 2008).

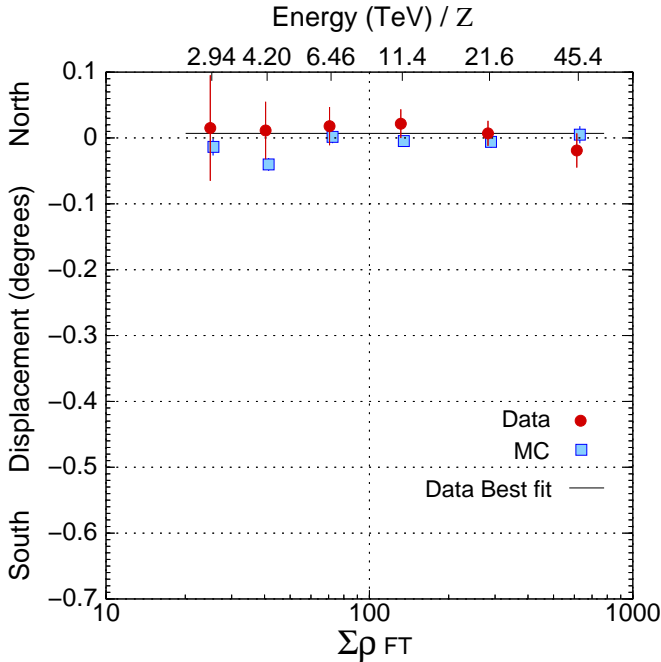


FIG. 5.— Dependence of shower size on the displacement of the moon's shadow in the north-south direction. The filled circles and open squares represent experimental data and the MC simulation, respectively. The solid line denotes the fitting to the experimental data assuming a constant function, resulting in $0^\circ 008 \pm 0^\circ 011$. The upper scale indicates the logarithmic mean of E/Z (TeV/Z) in each $\sum \rho_{\text{FT}}$ bin.

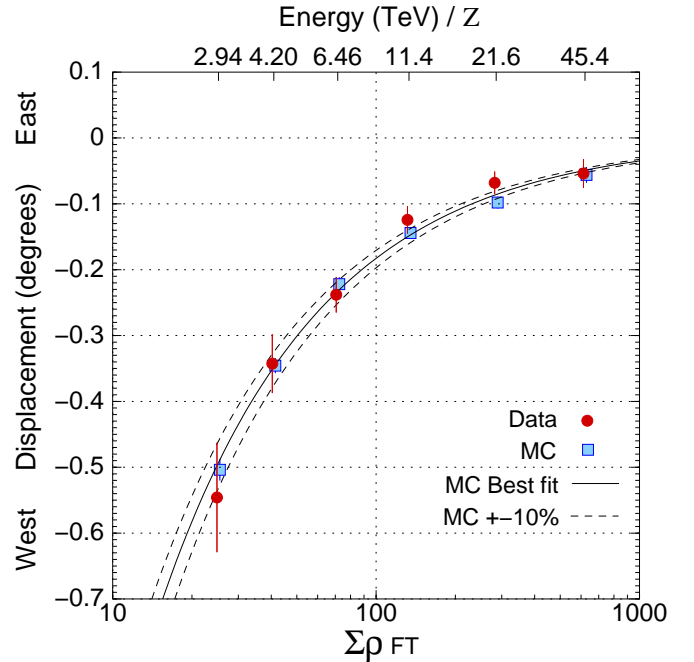


FIG. 6.— Dependence of shower size on the displacement of the moon's shadow in the east-west direction. The filled circles show the experimental data, and open squares represent the MC simulation. The solid curve is fitted to the MC events, and dashed curves show a $\pm 10\%$ deviation from the solid curve, respectively. The upper scale indicates the logarithmic mean of E/Z (TeV/Z) in each $\sum \rho_{\text{FT}}$ bin.

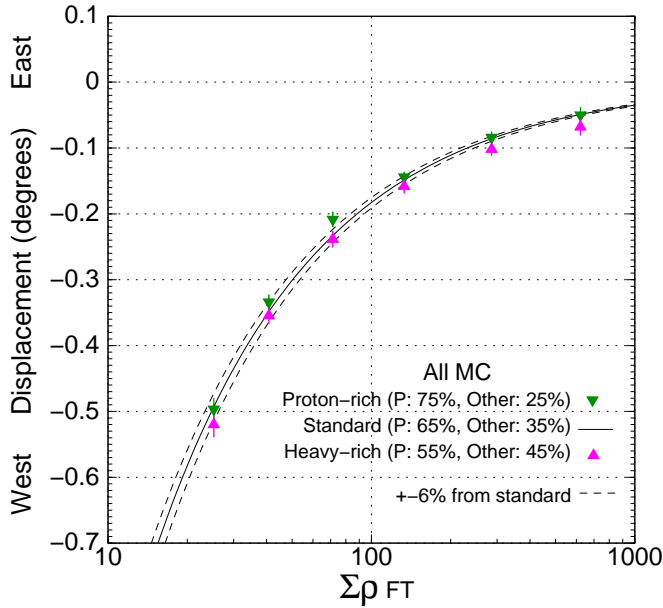


FIG. 7.— Dependence of shower size on the displacement of the moon’s shadow in the east-west direction by the MC simulation for the different primary composition models. The filled circles and open squares show the experimental data and MC simulation, respectively. The solid curve denotes the best-fit curve for the same standard composition ratio as in Fig. 6 (65% P after triggering by the Tibet-III array, where P means protons). The dashed curves show a 6% shift, corresponding to $\sigma_{\text{syst}1}$, from the solid curve (see text). The downward and upward triangles are the simulated results for the proton-rich model (P:75%), and for the heavy-rich model (P:55%), respectively.

component, so that the proton ratio is artificially varied by $\pm 10\%$ from a standard chemical composition without changing their spectral index, while the other components heavier than helium are varied by $\mp 10\%$ in total. Figure 7 shows the results for the composition dependence of primary cosmic rays. The downward triangles are the results obtained by the proton-rich model (75% protons after triggering by the Tibet-III array), while the upward triangles are the ones for the heavy-rich model (P:55%). These models are fitted by equation (3). We then obtain $\sigma_{\text{syst}1} = \pm 6\%$ for the systematic error due to the difference in chemical composition, as shown by the dashed curves in Figure 7. Another systematic uncertainty is caused by the difference between hadronic interaction models. Figure 8 compares the results for the hadronic interaction model dependence by QGSJET with those obtained by SIBYLL. It is found that the results by the SIBYLL model can be well fitted by equation (3) obtained using the QGSJET model. We then obtain $\sigma_{\text{syst}2} = 6\%$ difference between two models. Finally, the difference in the energy dependence of the moon’s shadow between the experimental data and the MC events is estimated to be $+4.5\% (\pm 8.6_{\text{stat}} \pm 6_{\text{syst}1} \pm 6/2_{\text{syst}2})\%$. This value is within the statistical and systematic errors. Hence, the absolute energy scale error in the Tibet-III array is estimated to be smaller than $12\% = \sqrt{\Delta R_E^2 + \sigma_{\text{stat}}^2 + \sigma_{\text{syst}1}^2 + (\sigma_{\text{syst}2}/2)^2}$ in total averaged from 3 to 45 (TeV/Z).

3.5. On the Energy Estimation of γ -Ray Showers

We established a new calibration method of the absolute energy scale for cosmic rays based on the moon’s

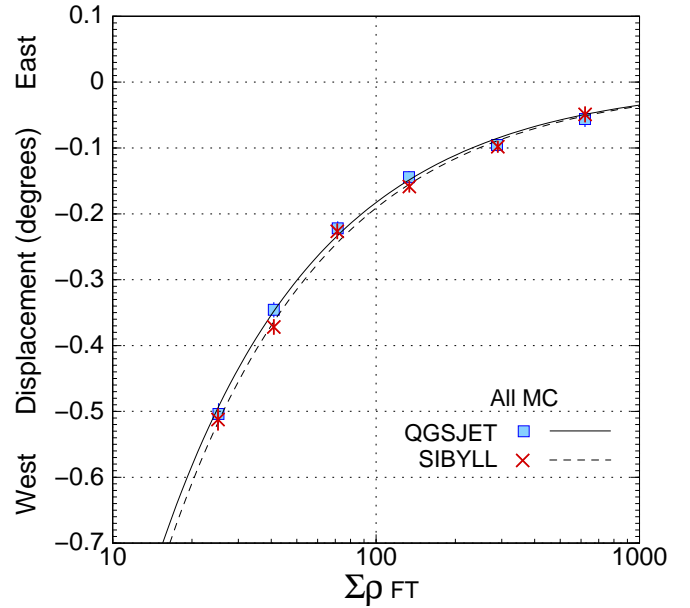


FIG. 8.— Dependence of shower size on the displacement of the moon’s shadow in the east-west direction by the MC simulation for different hadronic interaction models. The open squares and cross marks are the results obtained by the QGSJET and SIBYLL models, respectively. The solid and dashed curves are the best-fit results assuming the QGSJET and SIBYLL models, respectively.

shadow analysis as described above. The air shower induced by the primary cosmic ray consists of high-energy hadronic and electromagnetic cascades. Although several plausible hadronic interaction models are prepared in the MC simulation, there still remain dependence between these models. Therefore, the energy reconstruction from the air-shower size depends on hadronic interaction models and also the primary chemical composition models. These systematic errors were adequately taken into account in the absolute energy scale error in this paper. On the other hand, the air shower induced by the primary γ -ray is predominated by the theoretically well-known electromagnetic cascades, because the photon cross section for hadronic interactions is approximately two orders of magnitude smaller than that for the pair creation process. Hence, we naturally expect that the absolute energy scale error for γ -rays is smaller than 12% which is deduced from the moon’s shadow observed in the cosmic rays described in §3.4. In the next section, we will provide reliable results on the multi-TeV γ -ray observation from the Crab Nebula with the Tibet-III air shower array finely tuned by the cosmic-ray moon’s shadow.

4. MULTI-TeV γ -RAY OBSERVATION FROM THE CRAB

4.1. Analysis

In order to extract an excess of TeV γ -ray events coming from the direction of the Crab Nebula ($\alpha = 83^\circ 63'$, $\delta = 22^\circ 02'$), we adopt the same method as used in the Mrk 421 analysis in our previous work (Amenomori et al. 2003). We call it the equi-zenith angle method, which is used also for the moon’s shadow analysis described in §3.1. The background is estimated by the number of events averaged over eight off-source bins with the same angular radius as the on-source bin, at the same zenith angle, recorded at the same time intervals as the on-source bin. The nearest two off-source

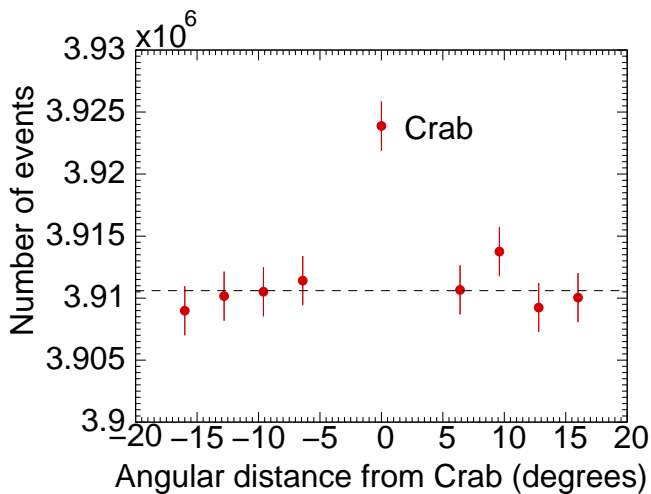


FIG. 9.— Number of observed air shower events with $\sum \rho_{\text{FT}} > 10^{1.25}$ ($> \sim 1$ TeV) after event reduction for the observation time of 1318.9 detector live days as a function of angular distance from the Crab Nebula in the azimuthal direction.

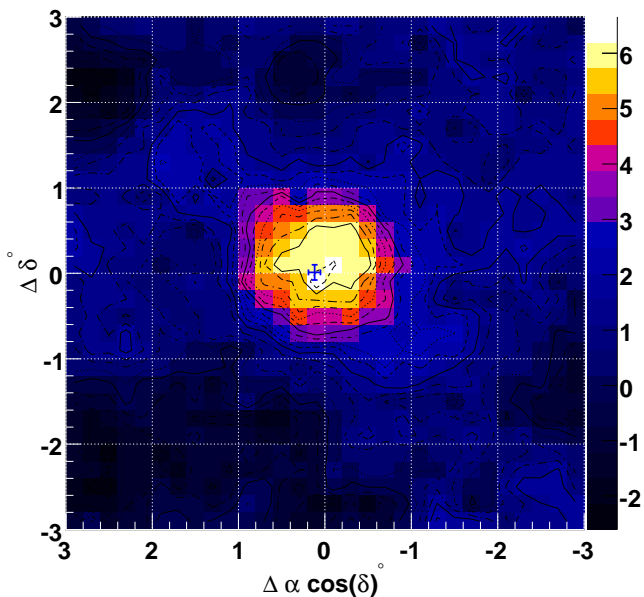


FIG. 10.— Contour map of significance distribution around the Crab Nebula ($\alpha = 83^\circ 63$, $\delta = 22^\circ 02$) for events with $\sum \rho_{\text{FT}} > 10^{1.25}$ ($> \sim 1$ TeV). A clear peak excess is seen at the center position $\Delta\alpha\cos(\Delta\delta) = \Delta\delta = 0^\circ$, where $\Delta\alpha$ and $\Delta\delta$ are the relative right ascension and declination, respectively, from the Crab Nebula. The cross mark indicates the pointing error by a point spread function fitting.

bins are set at an angular distance $6^\circ.4$ from the on-source bin to avoid a possible signal tail leaking into these off-source bins. Other off-source bins are located every $3^\circ.2$ step from the nearest off-source bins. The search window radius is expressed by $6.9/\sqrt{\sum \rho_{\text{FT}}}$ degrees as a function of $\sum \rho_{\text{FT}}$, which is shown to maximize the S/N ratio by MC study of γ -ray observation (Amenomori et al. 2003).

The number of events after the event reduction is plotted in Figure 9 as a function of angular distance from the Crab Nebula in the azimuthal direction. A clear peak of γ -ray signals from the Crab Nebula is seen at 6.3σ statis-

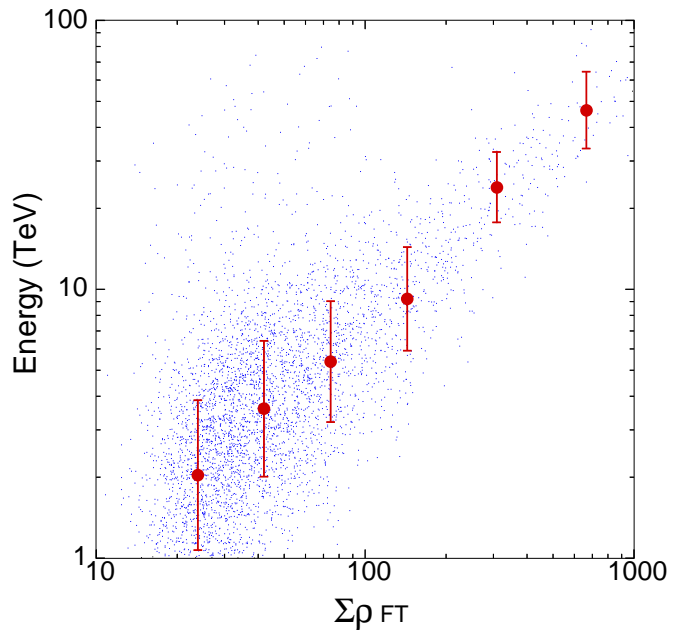


FIG. 11.— Scatter plot of the shower size $\sum \rho_{\text{FT}}$ and the energy of primary γ -rays, where a differential power-law spectrum of the form $E^{-2.6}$ starting at 0.3 TeV is assumed for primary γ -rays. For details, see text.

tical significance above the flat cosmic-ray background. Figure 10 is a significance map around the Crab Nebula. The peak excess is seen at the Crab Nebula position. The pointing error as shown by a cross mark in Figure 10 is estimated to be $\Delta\alpha = +0.13 \pm 0.08$ and $\Delta\delta = +0.01 \pm 0.09$ by the point spread function fitting. This is consistent with the Crab's position within statistical error. As difference between γ -ray induced air showers and cosmic-ray induced ones does not affect the pointing accuracy essentially, we estimate our pointing accuracy to be $0^\circ 011$ deduced from the moon's shadow analysis described in §3.3.

4.2. Monte Carlo Simulation of γ -Ray Observation from the Crab Nebula

The performance of the Tibet-III array has been studied by a full MC simulation using the CORSIKA code (Heck et al. 1998) for event generation in the atmosphere and the Epics code (Kasahara) for the response of the scintillation detector (Amenomori et al. 2003). These procedures are essentially the same as in the case for the moon's shadow described in §3.2. In the simulation for γ -ray observation from the Crab Nebula, primary γ -rays, assuming the energy spectrum of a power-law type in the energy region of 0.3 TeV to 1000 TeV, are thrown along the diurnal motion of the Crab Nebula in the sky. The air shower events generated are uniformly distributed over circle with a 300 m radius centered at the Tibet-III array. Shown in Figure 11 is the scatter plot of shower size $\sum \rho_{\text{FT}}$ and the energy of γ -rays coming from the Crab direction. The filled circles and error bars stand for the logarithmic mean and one-standard deviation of the logarithmic Gaussian, respectively. The one-event energy resolution is estimated to be approximately $(-40/+70)\%$ at 10 TeV, and approximately $\pm 100\%$ in the region of a few TeV.

The Crab Nebula can be treated as a point-like source

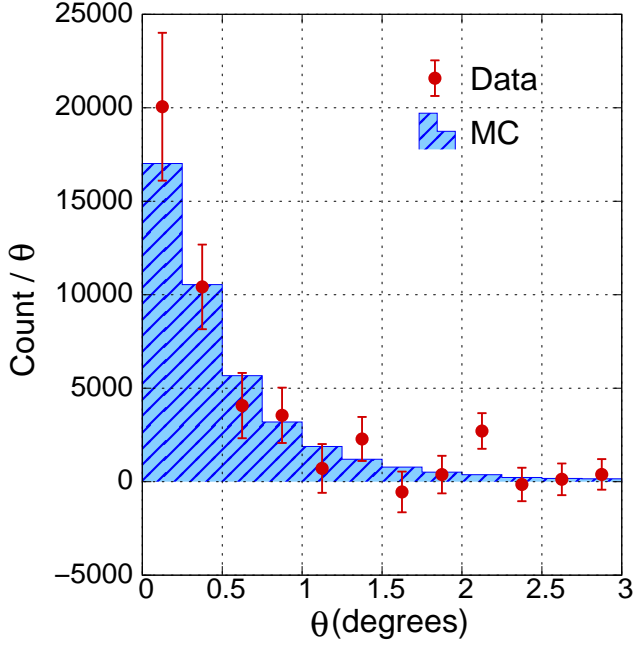


FIG. 12.— Distribution of excesses as a function of the opening angle relative to the Crab Nebula direction θ . The filled circles and shaded histograms stand for the experimental data and the MC events with $\sum \rho_{\text{FT}} > 10^{1.25}$ ($> \sim 1$ TeV), respectively.

at the TeV energy region. To investigate the point spread function of the Tibet-III array, we compared the θ distribution of the Crab Nebula between the experimental data and the MC events, where θ is the opening angle relative to the Crab Nebula direction. Figure 12 shows the distribution of the excess events as a function of θ for events with $\sum \rho_{\text{FT}} > 10^{1.25}$. The experimental data agree well with the MC simulation assuming the point-like source.

4.3. Energy Spectrum of γ -Rays from the Crab Nebula

The γ -ray flux from the Crab Nebula is estimated by assuming a power-law spectrum $f(E) = \alpha E^\beta$. The best-fit values α_0 and β_0 are given by minimizing a χ^2 function, changing α and β :

$$\chi^2 = \sum_{i=1}^6 \left(\frac{N_i^{\text{obs}} - N_i^{\text{sim}}(\alpha, \beta)}{\sigma_i^{\text{obs}}} \right)^2, \quad (4)$$

where N_i^{obs} , σ_i^{obs} and $N_i^{\text{sim}}(\alpha, \beta)$ are the observed number of excess counts, its error and the number of remaining MC events after the analysis assuming the spectrum $f(E) = \alpha E^\beta$, respectively, in the i -th $\sum \rho_{\text{FT}}$ bin among the six $\sum \rho_{\text{FT}}$ bins between $10^{1.25}$ and $10^{3.00}$ defined in §3.1. In order to estimate $N_i^{\text{sim}}(\alpha, \beta)$ in the same way as experimental data, simulated secondary particles are inputted to the detector response simulation. Then, we obtain the expected $N_i^{\text{sim}}(\alpha, \beta)$ for the i -th $\sum \rho_{\text{FT}}$ bin after the event reconstruction and event selections in the same way as experimental data. Here, the expected $N_i^{\text{sim}}(\alpha, \beta)$ includes the energy resolution effect by the detector response simulation.

Subsequently, the differential γ -ray flux for the i -th

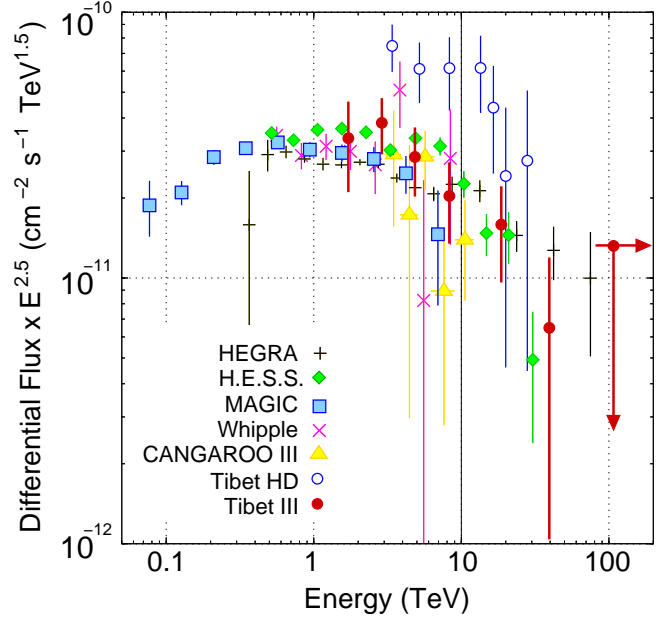


FIG. 13.— Differential energy spectrum of γ -rays from the Crab Nebula obtained using the data collected from 1999 November to 2005 November with the Tibet-III array in comparison with the results from IACTs: Whipple (Hillas et al. 1998), HEGRA (Aharonian et al. 2004), CANGAROO III (Enomoto et al. 2006), H.E.S.S. (Aharonian et al. 2006) and MAGIC (Albert et al. 2008). The Tibet-III upper limit is given at the 90% confidence level, according to a statistical prescription (Helene 1983).

$\sum \rho_{\text{FT}}$ bin is calculated by the following equation:

$$f_i(E_i) = \frac{N_i^{\text{obs}}}{N_i^{\text{sim}}(\alpha_0, \beta_0)} \frac{N_{\text{all}}^{\text{sim}}(\alpha_0, \beta_0)}{\int_{E_{\text{min}}^{\text{sim}}}^{\infty} E^{\beta_0} dE} \frac{E_i^{\beta_0}}{S_{\text{sim}} T_{\text{obs}}}, \quad (5)$$

where $N_{\text{all}}^{\text{sim}}(\alpha_0, \beta_0)$ denotes the total number of MC events generated at the top of the atmosphere along one diurnal motion assuming the spectrum $f(E) = \alpha_0 E^{\beta_0}$, $\int_{E_{\text{min}}^{\text{sim}}}^{\infty} E^{\beta_0} dE$ is the normalization factor of $N_{\text{all}}^{\text{sim}}(\alpha_0, \beta_0)$, $E_{\text{min}}^{\text{sim}}$ denotes the minimum energy of simulated air shower events (0.3 TeV), S_{sim} denotes the area of core location distribution by the simulation ($300 \text{ m} \times 300 \text{ m} \times \pi$), T_{obs} denotes the observation live time, and E_i denotes the representative energy defined as the logarithmic mean of the energy calculated by the MC simulation for the i -th $\sum \rho_{\text{FT}}$ bin.

Figure 13 shows the differential energy spectrum of the Crab Nebula observed by the Tibet-III array together with the spectra obtained by IACTs, including Whipple (Hillas et al. 1998), HEGRA (Aharonian et al. 2004), CANGAROO III (Enomoto et al. 2006), H.E.S.S. (Aharonian et al. 2006) and MAGIC (Albert et al. 2008). The differential flux for each $\sum \rho_{\text{FT}}$ bin is presented in Table 1. Finally, this energy spectrum is fitted by the least χ^2 method assuming $f(E) = \alpha(E/3 \text{ TeV})^\beta$, and then we obtain the differential power-law spectra as $(dJ/dE) = (2.09 \pm 0.32) \times 10^{-12} (E/3 \text{ TeV})^{-2.96 \pm 0.14} \text{ cm}^{-2} \text{ s}^{-1} \text{ TeV}^{-1}$ in the energy range of 1.7 TeV to 40 TeV. Note that the absolute energy scale error in the Tibet-III array is experimentally estimated to be smaller than $\pm 12\%$ by the moon's shadow observation described in §3.4. The

TABLE 1
LOGARITHMIC MEAN OF ENERGY AND DIFFERENTIAL FLUX FOR EACH $\sum \rho_{\text{FT}}$ BIN AS SHOWN IN FIG. 13.

$\sum \rho_{\text{FT}}$	Energy [TeV]	N_{ON}	ϵN_{OFF}	Differential Flux [$\text{cm}^{-2} \text{s}^{-1} \text{TeV}^{-1}$]
$10^{1.25} - 10^{1.50}$	1.71	1935499	1931547	$(8.72 \pm 3.25) \times 10^{-12}$
$10^{1.50} - 10^{1.75}$	2.89	1382356	1377139	$(2.70 \pm 0.643) \times 10^{-12}$
$10^{1.75} - 10^{2.00}$	4.84	444504	442074	$(5.52 \pm 1.60) \times 10^{-13}$
$10^{2.00} - 10^{2.33}$	8.29	134509	133362	$(1.03 \pm 0.348) \times 10^{-13}$
$10^{2.33} - 10^{2.67}$	18.6	21530	21138	$(1.06 \pm 0.417) \times 10^{-14}$
$10^{2.67} - 10^{3.00}$	39.5	3923	3844	$(6.64 \pm 5.57) \times 10^{-16}$
$> 10^{3.00}$	107	1558	1569	$< 1.10 \times 10^{-16}$

energy scale uncertainty corresponds to $(-28/+46)\%$ in the absolute γ -ray flux, assuming the spectral index -2.96 , which is our best-fit value. Our energy spectrum in this work is consistent with other observations made by IACTs, such as HEGRA and H.E.S.S., in the same energy range between 1.7 TeV and 40 TeV.

The previous flux measurement (Amenomori et al. 1999a), with the Tibet-HD array of 5,175 m² and an effective running time of 502.1 live days, is approximately double this measurement. In order to properly estimate the difference between the previous work and the present one, we give a re-fit to both data points from 2.8 TeV to 20 TeV in the overlapping energy region assuming a power-law spectrum. The previous (Tibet-HD) and present (Tibet-III) energy spectra are expressed as $(dJ/dE) = (5.04 \pm 0.94) \times 10^{-12} (E/3 \text{ TeV})^{-2.85 \pm 0.20} \text{cm}^{-2} \text{s}^{-1} \text{TeV}^{-1}$ and $(dJ/dE) = (2.35 \pm 0.49) \times 10^{-12} (E/3 \text{ TeV})^{-3.00 \pm 0.25} \text{cm}^{-2} \text{s}^{-1} \text{TeV}^{-1}$, respectively. The flux and spectral index differences between them are estimated to be $(2.69 \pm 1.06) \times 10^{-12} \text{cm}^{-2} \text{s}^{-1} \text{TeV}^{-1}$ and 0.15 ± 0.32 , respectively. As a result, the combined statistical deviation between them is calculated to be $\sqrt{(2.69/1.06)^2 + (0.15/0.32)^2} \sigma = 2.6\sigma$. Although we have updated the MC simulation in this analysis, we cannot find any systematics to explain this difference. Hence, we conclude that the higher flux observed in our previous measurement may have been caused by a statistical signal fluctuation.

4.4. Time Variability

We divided our dataset from 1999 November to 2005 November into six phases, as summarized in Table 2, to examine the time variability of the flux intensity. Each phase corresponds to approximately one calendar year. We used slightly different calibration parameters for each phase, because we usually calibrate the scintillation detectors of the Tibet air shower array late in the fall of every year. Unfortunately, some of the blank periods seen in Table 2 mostly coincide with the detector cali-

TABLE 2
DEFINITION OF SIX PHASES FROM 1999 NOVEMBER TO 2005 NOVEMBER AS SHOWN IN FIG. 14.

Phase	Period	Live Time [days]
1	Nov. 18, 1999 - Jun. 29, 2000	173.1
2	Oct. 28, 2000 - Oct. 11, 2001	283.7
3	Dec. 05, 2001 - Sep. 15, 2002	201.8
4	Nov. 18, 2002 - Nov. 18, 2003	259.1
5	Dec. 14, 2003 - Oct. 10, 2004	123.6
6	Oct. 19, 2004 - Nov. 15, 2005	277.6

bration periods, periods in which the air shower array was upgraded or when the data acquisition system was experiencing problems. The upper panel (a) in Figure 14 shows the time variability of the γ -ray fluxes from the Crab Nebula at 3 TeV. We found no evidence for the time variability of flux intensity from the Crab Nebula, as we can give a good χ^2 fit to these fluxes by a constant function ($\chi^2/d.o.f. = 6.55/5$), where *d.o.f.* means degrees of freedom. In order to check the possible systematics, the time variability of the deficit event rates of the moon's shadow is also demonstrated as shown by the middle panel (b) in Figure 14. The deficit event rates of the moon's shadow from 1999 November to 2005 November are very stable within a statistical error $\pm 6\%$ year by year. A fitting to the daily deficit event rate averaged over a phase assuming a constant function is consistent with a flat hypothesis ($\chi^2/d.o.f. = 4.82/5$). The lower panel (c) in Figure 14 shows the time variability of the north-south displacement of the moon's shadow, which is a reference to the absolute pointing error described in §3.2. It is also very stable within $\pm 0^\circ 04$ during our observation period, and is consistent with a flat hypothesis ($\chi^2/d.o.f. = 2.09/5$). These systematics, estimated

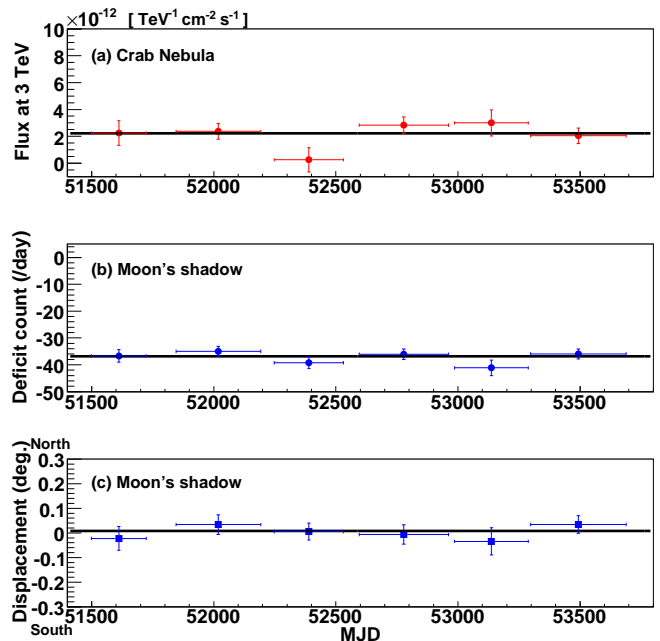


FIG. 14.— Time variability of the Crab Nebula and the moon's shadow observed by the Tibet-III array with $\sum \rho_{\text{FT}} > 10^{1.25}$ between 1999 November and 2005 November. (a): Differential flux of the Crab Nebula at 3 TeV. (b): Daily deficit event rate averaged over one phase of the moon's shadow. (c): North-south displacement of the moon's shadow.

from observations of the moon's shadow, are obviously negligible in the Crab Nebula observation.

4.5. Search for γ -Rays from the Crab Pulsar

The rotation period of the Crab pulsar is 33 ms, as inferred from radio, optical and X-ray observations. A pulsed emission with that rotation period at the GeV energy region has been detected by EGRET on board the CGRO satellite (Fierro et al. 1998), whereas several observations have reported no evidence for pulsed emissions greater than 10 GeV (Lessard et al. 2000; De Naurois et al. 2002; Aharonian et al. 2004; Aharonian et al. 2007; Albert et al. 2008). The emission models of high-energy pulsed γ -rays are mostly based on the outer gap (Cheng et al. 1986) and the polar cap (Daugherty & Harding 1982) models. The upscattered pulsed γ -ray flux is also calculated by the inverse-Compton process and the photon-photon absorption process assuming infrared photon field models. A model predicts an excessive flux around 1 \sim 10 TeV, depending on the infrared photon field models (Hirovani & Shibata 2001). Here, we present a search for pulsed γ -rays from the Crab pulsar at energies from a few TeV to 100 TeV using the Tibet-III array.

The arrival time of each event is recorded using a quartz clock synchronized with GPS, which has a precision of 1 μ s. For the timing analysis, all arrival times are converted to the solar system barycenter frame using the JPL DE200 ephemeris (Standish et al. 1982). The Crab pulsar ephemeris is calculated using the Jodrell Bank Crab Pulsar Monthly Ephemeris (Lyne et al. 1993; Lyne et al.). The corrected arrival time of each event is calculated to the rotation phase of the Crab pulsar, which takes into account of the period derivative \dot{P} of the period P month by month.

Figure 15 shows the distribution of events for each phase in two rotation periods of the Crab pulsar. The distribution is consistent with a flat distribution ($\chi^2/d.o.f. = 18.1/19$). No significantly pulsed signal is found in observations for events with $\sum \rho_{FT} > 10^{1.25}$ ($> \sim 1$ TeV). The phase analysis is performed for each $\sum \rho_{FT}$ bin to examine the energy dependence. Table 3 shows the statistical results by the Z_2^2 test (Buccheri et al. 1983), H test (De Jager 1994) and least χ^2 test. Almost all the statistical tests show that the phase distributions are uniform within a 3σ significance level. We estimate the 3σ flux upper limit on the pulsed emission from the Crab pulsar using the H test (De Jager 1994) as

$$x_{3\sigma} = (1.5 + 10.7\delta)(0.174H)^{0.17+0.14\delta} \times \exp\{(0.08 + 0.15\delta) \times (\log_{10}(0.174H))^2\}, \quad (6)$$

where δ is the duty cycle of the pulsed component, assuming δ is 21% for the Crab pulsar. Exposure from the Crab pulsar to the Tibet-III array is estimated using MC simulation, assuming the differential energy spectrum for γ -ray emission has a spectral index of -2.6 . Upper limits are compared to previous results inferred from other experiments, as shown in Figure 16.

5. SUMMARY AND PROSPECTS

We have been successfully operating the Tibet-III air shower array at Yangbajing in Tibet, China since

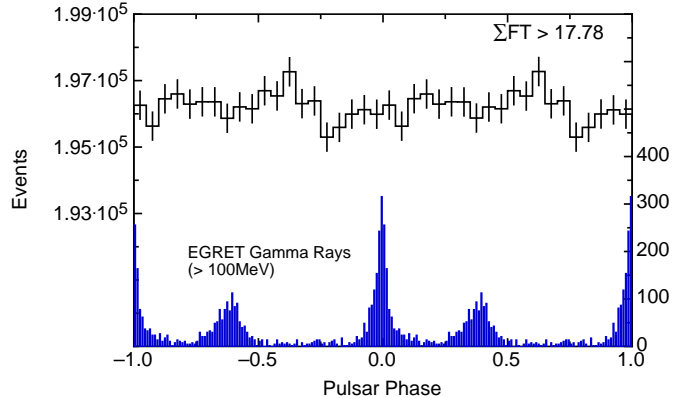


FIG. 15.— Distribution of the event phase of the Crab pulsar. Phase 0 is defined using the timing solution derived from the main pulse of the radio observations. Upper plot shows our result for events with $\sum \rho_{FT} > 10^{1.25}$ ($> \sim 1$ TeV). Lower plot shows the γ -ray phase histogram above 100 MeV, as measured by EGRET (Fierro et al. 1998).

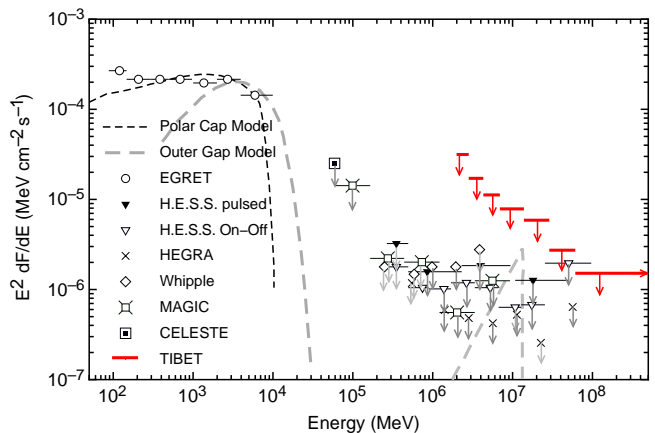


FIG. 16.— Upper limits on the pulsed γ -ray flux from the Crab pulsar observed by the Tibet-III array (arrows with thick solid line), together with results from Whipple (Lessard et al. 2000), CELESTE (De Naurois et al. 2002), HEGRA (Aharonian et al. 2004), H.E.S.S. (Aharonian et al. 2007) and MAGIC (Albert et al. 2008). The long-dashed curve and dashed curve represent the fluxes expected from the outer gap and polar cap models, respectively.

TABLE 3
RESULTS OF STATISTICAL TESTS FOR PULSED EMISSIONS. χ^2 -, Z_2^2 - AND H -TEST (PROBABILITIES) ARE CALCULATED FOR A FLAT PHASE DISTRIBUTION.

$\sum \rho_{FT}$	$\chi^2/d.o.f.$	Z_2^2	H
$10^{1.25} - 10^{1.50}$	0.97 (0.49)	9.62 (0.047)	9.62 (0.021)
$10^{1.50} - 10^{1.75}$	1.21 (0.24)	7.64 (0.11)	7.64 (0.047)
$10^{1.75} - 10^{2.00}$	0.81 (0.70)	2.54 (0.64)	4.49 (0.17)
$10^{2.00} - 10^{2.33}$	0.35 (0.96)	2.30 (0.68)	6.14 (0.086)
$10^{2.33} - 10^{2.67}$	1.41 (0.11)	9.68 (0.046)	14.56 (0.0030)
$10^{2.67} - 10^{3.00}$	0.80 (0.71)	3.67 (0.45)	6.09 (0.088)
$> 10^{3.00}$	0.60 (0.91)	1.11 (0.89)	4.48 (0.17)
$> 10^{1.25}$	0.95 (0.52)	8.41 (0.078)	8.87 (0.029)

1999. Using the dataset collected by this array from 1999 November through 2005 November, we obtained the differential energy spectrum of γ -rays from the Crab Nebula as $(dJ/dE) = (2.09 \pm 0.32) \times 10^{-12} (E/3 \text{ TeV})^{-2.96 \pm 0.14} \text{ cm}^{-2} \text{ s}^{-1} \text{ TeV}^{-1}$ in the energy range of 1.7 TeV to 40 TeV. This result is consistent with data obtained by IACTs, and is statistically consistent with our previous result within 2.6σ . No evidence is found for time variability of flux intensity from the Crab Nebula at multi-TeV energies in comparison with the long-term stability of the moon's shadow. We also searched, unsuccessfully, for pulsed γ -rays from the Crab pulsar at multi-TeV energies.

In this paper, we have carefully analyzed the moon's shadow observed with the Tibet-III array to calibrate the energy of primary cosmic rays directly. In general, this energy is indirectly estimated by measuring shower size in air shower experiments. The cosmic-ray beams coming from the moon's direction are bent by the geomagnetic field, so that the moon's shadow should shift to the west depending on the primary energy. We tried to directly estimate the primary energy by measuring the displacement of the moon's shadow. This energy scale estimation is the first attempt and obtained that the systematic error in the absolute energy scale observed by the Tibet-III array is estimated to be less than $\pm 12\%$ at energies around 10 TeV. The array's systematic pointing error is also estimated to be smaller than $0^\circ.011$. The long-term stability of the deficit rate of the moon's shadow was within a statistical error $\pm 6\%$ year by year, thus confirming the stability of the array operation. This calibration method is very unique and will be important to ground-based TeV γ -ray observations.

In the near future, we will set up a 10,000 m² water-Cherenkov-type muon detector (MD) array in the ground beneath the Tibet air shower (AS) array (Amenomori et al. 2007b; Amenomori et al. 2007c; Amenomori et al. 2007d). This Tibet MD array will significantly improve γ -ray sensitivity of the Tibet air shower array above 10 TeV by means of γ /hadron separation based on counting the number of muons accompanying each air shower. The energy spectrum of the Crab Nebula can be surely measured up to several hundred TeV, if extended, with a low background level, using the Tibet AS+MD array. This new array will enable us to survey not only the known sources but also new sources in the northern sky above 10 TeV, and may be superior to IACTs for observing diffuse γ -ray sources (Amenomori et al. 2006; Abdo et al. 2007) and diffuse γ -rays from the galactic plane (Amenomori et al. 2002; Atkins et al. 2005), owing to its wide field of view and high rejection power for hadronic showers.

The collaborative experiment of the Tibet Air Shower Arrays has been performed under the auspices of the Ministry of Science and Technology of China and the Ministry of Foreign Affairs of Japan. This work was supported in part by a Grant-in-Aid for Scientific Research on Priority Areas from the Ministry of Education, Culture, Sports, Science and Technology, by Grants-in-Aid for Science Research from the Japan Society for the Promotion of Science in Japan, and by the Grants from the National Natural Science Foundation of China and the Chinese Academy of Sciences.

REFERENCES

- Abdo, A. A., et al. 2007, *ApJ*, 664, L91
 Achard, P., et al. 2005, *Astroparticle Physics*, 23, 411
 Aharonian, F., et al. 2004, *ApJ*, 614, 897
 ———. 2006, *A&A*, 457, 899
 ———. 2007, *A&A*, 466, 543
 Albert, J., et al. 2008, *ApJ*, 674, 1037
 Alexandreas, D. E. 1991, *Phys. Rev. D*, 43, 1735
 Amenomori, M., et al. 1992, *Phys. Rev. Lett.*, 69, 2468
 ———. 1993, *Phys. Rev. D*, 47, 2675
 ———. 1994, *ApJ*, 415, L147
 ———. 1999a, *ApJ*, 525, L93
 ———. 1999b, *Advances in Space Research*, 23, 611
 ———. 2000a, *ApJ*, 541, 1051
 ———. 2000b, *ApJ*, 532, 302
 ———. 2002, *ApJ*, 580, 887
 ———. 2003, *ApJ*, 598, 242
 ———. 2005, *ApJ*, 633, 1005
 ———. 2006, *Science*, 314, 439
 ———. 2007a, *Astroparticle Physics*, 28, 137
 ———. 2007b, *Astrophysics and Space Science*, 309, 435
 ———. 2007c, *Proc. 30th Int. Cosmic Ray Conf.*, in press
 ———. 2007d, *Proc. 30th Int. Cosmic Ray Conf.*, in press
 ———. 2008, *ApJ*, 678, 1165
 Apanasenko, A. V., et al. 2001, *Astroparticle Physics*, 16, 13
 Asakimori, K., et al. 1998, *ApJ*, 502, 278
 Atkins, R., et al. 2003, *ApJ*, 595, 803
 ———. 2005, *Phys. Rev. Lett.*, 95, 251103
 Atoyan, A. M., & Aharonian, F. A., 1996 *A&AS*, 120, 453
 Buccheri, R., et al. 1983, *A&A*, 128, 245
 Cheng, K. S., Ho, C., & Ruderman, M. 1986, *ApJ*, 300, 500
 Clark, G. W. 1957, *Physical Review*, 108, 450
 Daugherty, J. K. & Harding, A. K. 1982, *ApJ*, 252, 337
 De Jager, O. C. 1994, *ApJ*, 436, 239
 De Jager, O. C., et al. 1996, *ApJ*, 457, 253
 De Naurois, M., et al. 2002, *ApJ*, 566, 343
 Enomoto, R., et al. 2006, *ApJ*, 638, 397
 Fierro, J. M., Michelson, P. F., Nolan, P. L., & Thompson, D. J. 1998, *ApJ*, 494, 734
 Heck, D., Knapp, J., Capdevielle, J. N., Shatz, G., & Thouw, T. 1998, *CORSIKA: A Monte Carlo Code to Simulate Extensive Air Showers (FZKA 6019)*(Karlsruhe: Forschungszentrum Karlsruhe)
 Helene, O. 1983, *Nucl. Instrum. Methods Phys. Res.*, 212, 319
 Hillas, A. M., et al. 1998, *ApJ*, 503, 744
 Hirotoni, K. & Shibata, S. 2001, *ApJ*, 558, 216
 Kasahara, K., <http://cosmos.n.kanagawa-u.ac.jp/EPICSHome/index.html>
 Lessard, R. W., et al. 2000, *ApJ*, 531, 942
 Li, T.-P., & Ma, Y.-Q. 1983, *ApJ*, 272, 317
 Lyne, A. G., Pritchard, R. S. & Smith, F. G. 1993, *MNRAS*, 265, 1003
 Lyne, A. G., Roberts, M. E. & Jordan, C. A, *JODRELL BANK CRAB PULSAR MONTHLY EPHEMERIS*, <http://www.jb.man.ac.uk/~{pulsar}/crab.html>
 Macmillan, S., et al. 2003, *Geophys. Journal Inter.*, 155, 1051
<http://www.ngdc.noaa.gov/IAGA/vmod/igrf.html>
 Sanuki, T., et al. 2000, *ApJ*, 545, 1135
 Standish, E. M., Jr. 1982, *A&A*, 114, 297
 Weekes, T. C. et al. 1989, *ApJ*, 342, 379